Article

Preparation and Adsorption Performance of Walnut Waste-Based Magnetic Activated Carbon with High Specific Surface Area

Resalat Yimin, Reyangul Abla, Gulbagar Dawut, Abdukader Abdukayum,* and Bin Xiong

Cite This: *ACS Omega* 2025, 10, 498–508

Read Online

ACCESS | Metrics & More | Article Recommendations

ABSTRACT: Magnetic activated carbon (MAC) derived from agricultural waste shows significant potential for the removal of norfloxacin (NOR) from wastewater. However, understanding the removal mechanisms, efficiency, and recyclability of MAC produced from walnut green husk and ferrocene for NOR remains a challenge. In this study, walnut green husk-based MAC (HQP-MC) was synthesized, and changes in surface functionality, mechanisms for NOR removal, and major influencing factors were investigated. The results indicated that HQP-MC predominantly features a mesoporous structure with a diverse array of surface functional groups, including $-OH$, NH_2, $C=O$, and $C-O$. Additionally, HQP-MC demonstrates a remarkable adsorption capacity for NOR, achieving 226.8 $mg·g^{-1}$ at 298 K and pH 7.0 under various substrates and experimental conditions. This high capacity can be attributed to a significantly enhanced specific surface area and pore volume, which increased by factors of 2.40 and 2.46, respectively, compared with pristine activated carbon. Moreover, HQP-MC exhibited an exceptional saturation magnetic strength of 11.5 $emu·g^{-1}$, along with a reusability rate of 80.5% after ten cycles. The adsorption kinetics were effectively described by the pseudo-second-order model and the Langmuir isotherm model. This study provides valuable insights into the sustainable development of magnetic adsorbent materials derived from agricultural waste and their applications in wastewater decontamination.
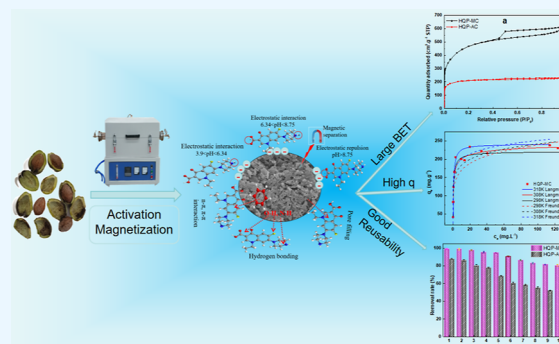
1. INTRODUCTION

Drug residues in water have emerged as a significant global concern for both environmental integrity and public health. Recent trends indicate a consistent rise in the variety and concentration of antibiotics identified in aquatic systems. Furthermore, the persistence of these residual antibiotics can contribute to the development of bacterial resistance, which poses considerable risks to human health through potential transmission via the food supply.[1] Norfloxacin (NOR) is a third-generation fluoroquinolone that has been extensively employed in the fields of medicine,[2,3] animal husbandry, and aquaculture because of its favorable pharmacokinetic characteristics, broad-spectrum antibacterial activity, potent antibacterial properties, and low toxic side effects.[3] As is known, NOR has been widely used in many countries. For instance, in China, the annual consumption of NOR amounts to 1820 tons.[4] However, only 10% to 60% of NOR is absorbed by organisms.[5] The majority of fractions that have been excreted into the environment as predrugs cause water, air, and soil pollution, making them a common organic pollutant in water. This has caused potential ecological risks and endangered human health.[6] As reported by some researchers, the concentration of NOR residues detected in animal manure ranged from 1.886 to 225 $mg·kg^{-1}$.[7] Consequently, the development of cost-

effective and efficient methods for the removal of NOR prior to their release into the environment has garnered significant interest. Currently, NOR or other pharmaceuticals are eliminated from aquatic environments through various methods, including oxidation, ultraviolet degradation, reverse osmosis, and nanofiltration.[8−13] Nevertheless, the economic viability of these systems has been hindered by challenges, such as the generation of hazardous sludge, incomplete removal of contaminants, high capital and operational expenses, and the requirement for specialized personnel for operation and maintenance. Consequently, the presence of pharmaceuticals in water underscores the need for more advanced purification technologies to obtain clean water. However, current methodologies are limited by their substantial costs, low reusability, and disposal challenges.[14] To address this issue, it is essential to develop a long-term solution that meets current demands

while minimizing the environmental impact. This solution should be grounded in social, techno-economic, and environmental considerations and implemented in a sustainable manner. Employing cost-effective and sustainable adsorbents prevents the direct disposal of pharmaceuticals into water bodies. Adsorption-based decontamination has been widely applied due to their low cost, simple preparation, easy industrialization, high adsorption efficiency, environmental friendliness, and straightforward technique for eliminating pollutants.[15] A substantial body of research demonstrates that the remarkable stability, large specific surface area, and rich pore structure of activated carbon (AC) contribute to its widespread utilization in the remediation of water pollutants, including heavy metals,[16,17] gaseous substances,[18] pharmaceuticals,[19-22] dyes,[23-25] and various other contaminants.

Despite the established methodologies for the preparation of activated carbon (AC), its limited recyclability results in a significant energy expenditure. To address this issue, researchers have effectively synthesized magnetic activated carbon (MAC),[26-28] which contributes to decreased energy consumption and costs due to its enhanced recyclability. Various methods have been reported to make MAC, including ball milling, coprecipitation, wet-dipping, and hydrothermal treatment with various magnetizing agents such as iron, cobalt, nickel, manganese, and their salts.[29] Liu et al.[30] reported a preparation method for magnetic biochar through one-step pyrolysis. They utilized it to remove NOR with a magnetic strength of 3.57 emu·g^{-1}, reaching equilibrium in 8 h, with a maximum adsorption capacity of 166 mg·g^{-1}. Wang et al.[4] produced γ-Fe$_2$O$_3$@BC and used it to remove NOR with a high magnetic strength of 30.60 emu·g^{-1} and a maximum adsorption capacity of 5.52 mg·g^{-1} within 2 h. However, current methods encounter various issues, such as either a low magnetic strength or low adsorption capacity. After magnetization, the BET surface area and pore volume decrease because some pores are blocked by magnetic particles.[31] Mohan et al.[21] developed MAC from almond shells and used it for trinitrophenol removal from water. They found that the specific surface area (S_{BET}) of MAC (527 m^2·g^{-1}) was lower compared to nonmagnetic activated carbon (733 m^2·g^{-1}) due to pore blocking. It is necessary to find an improved method for magnetization that offers strong magnetic strength, high adsorption capacity, and minimal or no pore blocking.

Agricultural waste is characterized by its abundance, renewability, and low-cost availability, rendering it an ideal resource for the production of carbon-based materials such as graphene oxide, carbon nanotubes, carbon dots, and activated carbon.[32-35] The utilization of these materials has the potential to mitigate waste management and disposal expenses. Walnut is a significant category of nuts and woody oilseed tree species, possessing considerable economic importance. The green husk of the walnut, as depicted in Figure 1, constitutes a substantial external layer of immature walnuts, comprising approximately 50% of the total weight of the walnut.[36] The generation of byproducts from walnut green husk surpasses that of walnut kernels. Nevertheless, the lack of specialized technical methods for prompt processing results in considerable resource waste and environmental pollution. Dealing with agricultural waste from walnuts has always been an urgent issue to address during the mature season (in October). One effective way to address the above issue is by transforming walnut waste into MAC with a high specific surface area, stability, low cost, and environmentally friendly properties, thereby achieving the goal of

Figure 1. Walnut green husk.

"treating pollutants with waste and turning waste into treasure."

In this paper, HQP-MC with magnetic response and high specific surface area was prepared using pyrolysis with walnut green husk and ferrocene as raw materials. As a result, HQP-MC offers advantages, such as a high specific surface area, a well-developed pore structure, rich surface functional groups, and stable chemical properties. This material exhibits an excellent adsorption capacity for NOR. Furthermore, the magnetic response enables HQP-MC to achieve rapid separation speed and excellent recyclability. Therefore, this result offers an effective solution for dealing with fluoroquinolones and other pollutants that share similar physical and chemical properties in water. It also presents an efficient method for using agricultural residues.

2. MATERIALS AND METHODS

2.1. Materials. Walnut green husks were gathered in October in Shufu, Xinjiang, China. Subsequent to the elimination of dust, the item was allowed to air-dry naturally. Ferrocene (AR) and potassium hydroxide (KOH, AR) were purchased from Macklin. Ethanol, hydrochloric acid (HCl, AR), and sodium hydroxide (NaOH, AR) were provided by the Xinjiang Key Laboratory of Novel Functional Materials Chemistry. Deionized water was used to prepare all of the solutions required for the experiment.

2.2. Preparation. *2.2.1. Preparation of HQP-AC.* After undergoing a series of processing steps including cleaning, drying, crushing, and sieving, the walnut green husk was activated with 1.7 mol·L^{-1} KOH solution for 12 h with stirring at 298 K. Subsequently, after being filtered and dried, the sample was placed in a tube furnace and heated up to 1073 K under nitrogen protection at a flow rate of 5 °C/min. Activation was conducted for 2.5 h, followed by a cooling process. The sample was then rinsed with deionized water until reaching a neutral pH and subsequently dried for 24 h at 373 K in a vacuum oven.

2.2.2. Preparation of HQP-MC. HQP-AC powder and ferrocene (m:m, 2:3) were mixed with the proper amount of ethanol (just submerge the solid mixture) and sonicated for 1 h to ensure thorough mixing. The mixture was placed in the crucible and then transferred to a tube furnace heated to 1073 K for 4 h under nitrogen protection at a flow rate of 5 °C/min. After being cooled to room temperature, the sample was washed with deionized water until neutral and then dried in a vacuum oven at 373 K for 24 h (Figure 2).

2.3. Characterization. The microstructure of the materials was observed by using a scanning electron microscope
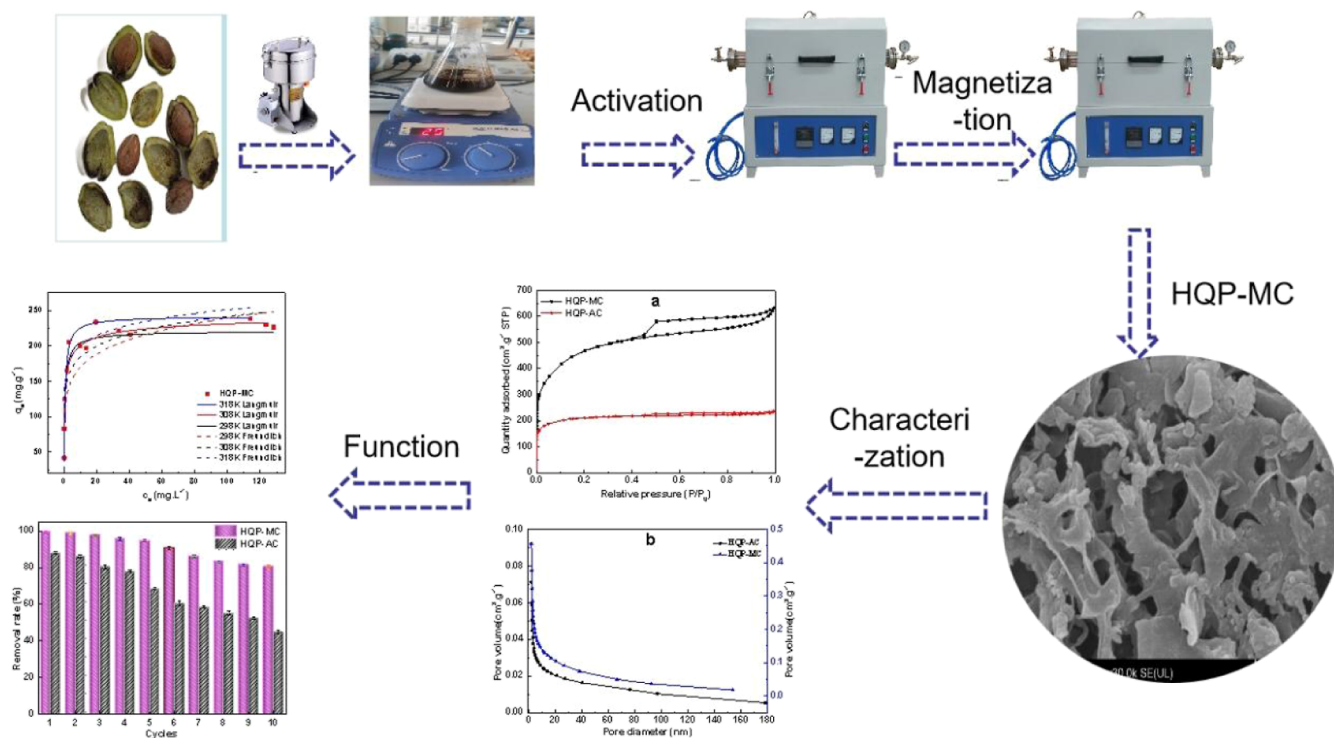
Figure 2. Diagram illustrating the preparation process and performance of HQP-MC.

(Hitachi, SU8010). Functional groups of the materials were determined by using a Fourier transform infrared spectrometer (Hitachi, FTIR-200) with a wavenumber range of 4000−400 cm^{-1}. The hysteresis loop of the materials was measured using a vibrating sample magnetometer (Lake Shore, 7404) within a magnetic field range from −2T to 2T at room temperature. Phase composition of the materials was examined using X-ray diffractometry (XRD) with 2θ ranging from 20° to 80° (Bruker, D8 ADVANCE). N$_2$ adsorption isotherms of the materials were tested by using a surface area and pore size analyzer (Micromeritics, 3Flex Version 5.00). The specific surface area, pore size, and pore volume of the sample were determined using the BET, BJH, and HK methods, respectively.

2.4. Adsorption Experiment. The influence of various initial pH values (3.0−13.0), adsorbent dosage (0.4 g·L^{-1}−2.0 g·L^{-1}), adsorption time (0−250 min), reaction temperature (298K, 308 K, and 318 K), and concentration of NOR (50−400 mg·L^{-1}) was studied by conducting batch experiments. The effect of different pH was studied at 298 K. Sixty milligrams of HQP-MC were added to 50 mL of NOR solution with a concentration of 100 mg·L^{-1}. The mixture was placed in a water bath oscillator and allowed to react for 10 h. The pH of the solution was adjusted by adding 0.1 mol·L^{-1} of NaOH or HCl. The magnetic adsorbent was separated by adding an external magnet in the following experiments. The concentration of NOR before and after adsorption was analyzed using an ultraviolet−visible spectrophotometer (SHIMADZU, UV-2600) at a wavelength of 272 nm. The adsorption capacity and removal rate of NOR by HQP-AC/HQP-MC were calculated using the following formulas, respectively.[37]

$$q_e = \frac{(c_o - c_e)V}{m} \tag{1}$$

$$w = \frac{(c_o - c_e)}{c_o} \times 100\% \tag{2}$$

where q_e (mg·g^{-1}) and w (%) represent the adsorption capacity and removal rate of HQP-AC/HQP-MC for NOR, respectively, c_o (mg·L^{-1}) and c_e (mg·L^{-1}) denote the initial and equilibrium concentration of the NOR solution, respectively, V (L) stands for the volume of the NOR solution, and m (g) represents the mass of HQP-AC/HQP-MC. Langmuir (3) and Freundlich (4) models were applied to study the adsorption isotherm.

$$1/q_e = 1/(q_m k_L c_e) + 1/q_m \tag{3}$$

$$q_e = k_F c e^{1/n} \tag{4}$$

where k_L (L·mg^{-1}) is the Langmuir constant, q_m (mg·g^{-1}) is the maximum adsorption capacity, k_F (mg/(L$^{1/1-n}$·g)) is the Freundlich constant related to adsorption capacity, and n is an empirical parameter related to adsorption strength.[4] Pseudo-first (5), pseudo-second-order (6), and Elovich model (7) kinetics were used to study the mass transfer mechanism of the adsorption process.

$$\lg(q_e - q_t) = \lg q_e - k_1 t/2.303 \tag{5}$$

$$t/qt = 1/k_2 q_e^2 + t/q_e \tag{6}$$

$$q_t = 1/\beta \ln(\alpha\beta t + 1) \tag{7}$$

where k_1 (min) and k_2 (g/(mg·min)) are the reaction rate constants for the pseudo-first-order and pseudo-second-order models, respectively, the variable q_t (mg·g^{-1}) represents the adsorption capacity at a specific time, α (mg/(g·min)) is the initial adsorption rate constant, and β (g·min^{-1}) is the extent of surface coverage.[38] The thermodynamic parameters were calculated using formulas 8−10 to estimate the thermody-
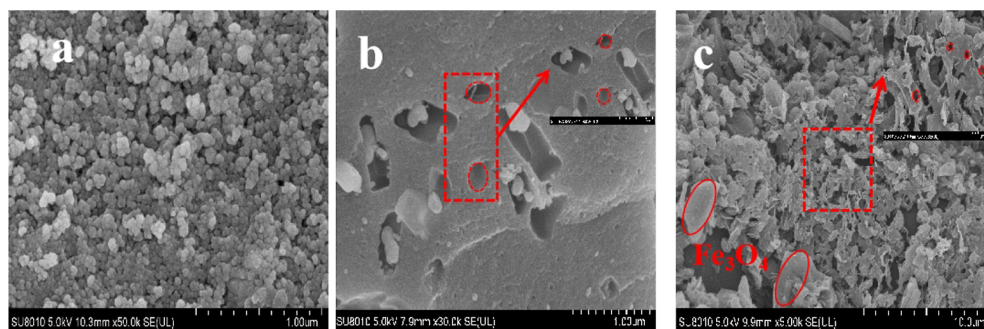
Figure 3. SEM images of Fe$_3$O$_4$ (a), HQP-AC (b), and HQP-MC (c).

namic behavior of NOR adsorption onto HQP-AC and HQP-MC.

$$K_d = q_e/c_e \qquad (8)$$

$$\Delta G = \Delta H - T\Delta S \qquad (9)$$

$$\ln K_d = -\Delta H/TR + \Delta S/R \qquad (10)$$

where $\triangle G$ represents Gibbs free energy (kJ·mol^{-1}), $\triangle H$ denotes enthalpy (kJ·mol^{-1}), $\triangle S$ signifies entropy (J·mol^{-1}·K^{-1}) and R is the universal gas constant 8.314 (J·mol^{-1}·K^{-1}), T stands for temperature (K), and K_d is the distribution coefficient for adsorption.[39]

3. RESULTS AND DISCUSSION

3.1. Characterization Results. The surface morphologies of HQP-AC and HQP-MC examined by SEM are shown in Figure 3. The surface of HQP-AC is quite rough and exhibits an irregular pore structure. The surface of HQP-MC is highly porous, featuring numerous irregular wrinkled structures that facilitate the provision of more adsorption sites. After activation with KOH and treatment with ferrocene, the porosity of the MAC derived from walnut green husk is enhanced. This unique structure and morphology enable HQP-MC to have a higher surface area and better adsorption performance. BET test results and adsorption performance further confirm this finding.

XRD analysis was conducted to identify the presence of Fe$_3$O$_4$ in HQP-MC. The XRD spectra of Fe$_3$O$_4$, HQP-AC, and HQP-MC are shown in Figure 4. There are two broad diffraction peaks in the ranges of 20−30° and 40−50° for HQP-AC, which can be assigned to (002) and (100) diffraction peaks, indicating graphitic carbon (JCPDS: 75−2078).[40] The XRD patterns of HQP-MC exhibit obvious diffraction peaks at 30.1°, 35.5°, 43.1°, 53.7°, 57.1°, and 62.8°; they can be assigned to the (220), (311), (400), (422), (511), and (440) crystal structure of Fe$_3$O$_4$, according to the standard card (JCPDS: 75−0033).[41] This confirms that HQP-MC has good purity and crystallinity.

FTIR was applied to verify the structural composition and functional groups present in the materials. The absorption peak at 579 cm^{-1}, as illustrated in Figure 5, is exclusively associated with the Fe−O stretching vibration in HQP-MC, confirming the successful magnetization process. The broad band with high intensity appearing at about 3450 cm^{-1} is associated with the elongation vibration of the functional groups −OH and −NH$_2$. The band of high intensity around 1627 cm^{-1} is attributed to the stretching vibration of C=O due to carboxyl. The peak around 1400 cm^{-1} should be the
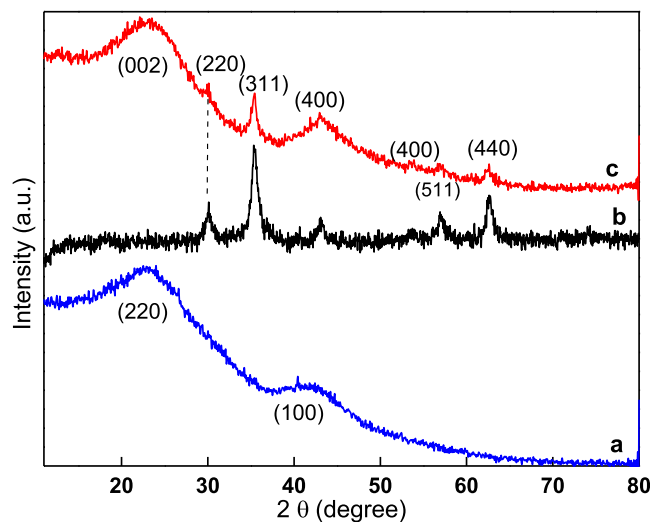
Figure 4. XRD patterns of HQP-AC (a), Fe$_3$O$_4$ (b), and HQP-MC (c).

bending vibration of carbon hydrogen bonds.[41−43] The peak examined at 1040 cm^{-1} is the stretching band of C−O from the carboxylic group.[44] The sharp band at 872 is the bending vibration of =C−H in aromatic hydrocarbon. These various functional groups are more favorable to the adsorption process.

The magnetic responsiveness of HQP-AC and HQP-MC was evaluated through VSM analysis conducted at room temperature. The findings are illustrated in Figure 6. The hysteresis curve of HQP-AC demonstrates a linear trend without hysteresis and magnetization, suggesting the absence of magnetic characteristics in activated carbon derived from walnut green husk. The magnetic saturation strength of HQP-MC reached 11.5 emu·g^{-1}, and the hysteresis loop is symmetric with zero coercivity. Therefore, it exhibits superparamagnetism and demonstrates a strong magnetic response to an external magnet. After the external magnetic field is removed, the magnetic adsorbent demagnetizes and ensures high dispersion in the system. Due to its magnetic properties, the HQP-MC was separated within 15 s by an external magnet, thereby increasing the recyclability of the absorbents.[27] The strong magnetic properties facilitate the rapid separation of HQP-MC from the system without the need for suction and filtration, greatly reducing the experimental time.

The N$_2$ adsorption−desorption isotherms and BJH pore size distribution profiles of HQP-AC and HQP-MC are clearly illustrated in Figure 7 and Table 1. The isotherms exhibit rapid N$_2$ adsorption rates at low relative pressures (P/P_0) between 0 and 0.1, indicating the presence of micropores. At higher
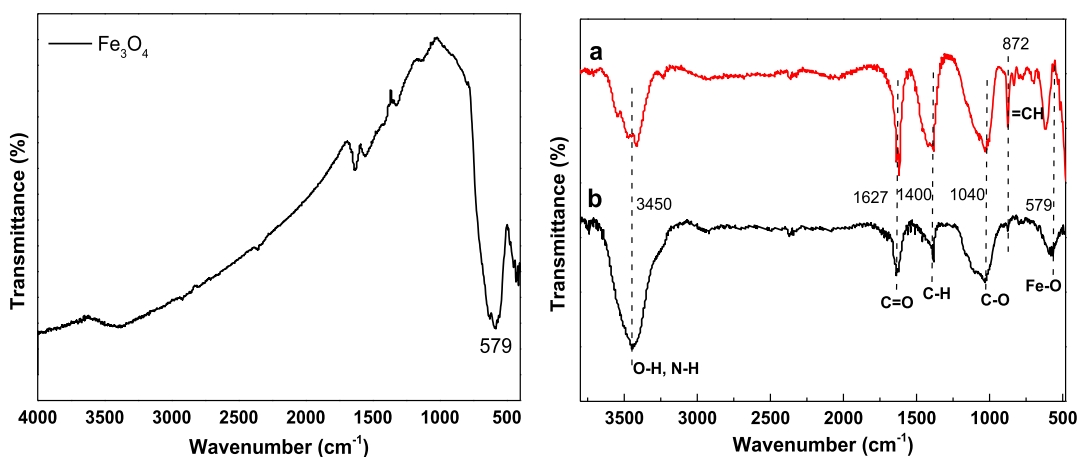
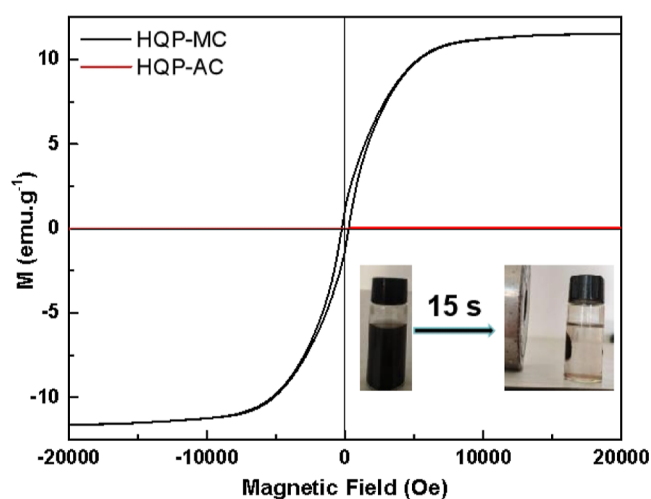**Figure 5.** FTIR spectra of Fe$_3$O$_4$ and HQP-AC (a) and HQP-MC (b).

Figure 6. Magnetization hysteresis loops of HQP-AC and HQP-MC.

Figure 7. N$_2$ adsorption−desorption isotherms (a) and pore size distribution profiles (b) of HQP-AC and HQP-MC.

relative pressures ($P/P_0 > 0.4$), distinct hysteresis loops are observed without overlap between the adsorption and desorption curves, suggesting the presence of mesopores, with the adsorption type classified as type I.[45,46] Moreover, the BET surface area of HQP-MC (1541.6 m^2·g^{-1}) was found to be 2.40 times greater than that of HQP-AC (648.9 m^2·g^{-1}). This discrepancy suggests that ferrocene, during the pyrolysis process, activates and enlarges the pores of activated carbon, thereby increasing the specific surface area and pore volume of magnetically activated carbon without pore blockage. This enhancement can lead to a high adsorption capacity, as the BET surface area is a critical factor in the adsorption capacity of absorbents.[39]

The pore size distribution analysis conducted using the BJH method, as illustrated in Figure 7b, indicated that the pore size distribution patterns of HQP-AC and HQP-MC primarily focused on the ranges of 1−15 and 1−10 nm, respectively. This suggests the existence of micropores (with an average pore diameter (D_{ap}) below 2 nm) and mesopores (D_{ap} between 2 and 50 nm), with a little presence of macropores (D_{ap} exceeding 50 nm). The total pore volume of HQP-MC (1.6868 cm^3·g^{-1}) was notably higher, being 2.46 times that of HQP-AC (0.6857 cm^3·g^{-1}). These findings suggest enhanced adsorption potential for NOR, as the adsorption capacity of adsorbents toward contaminants is directly linked to their
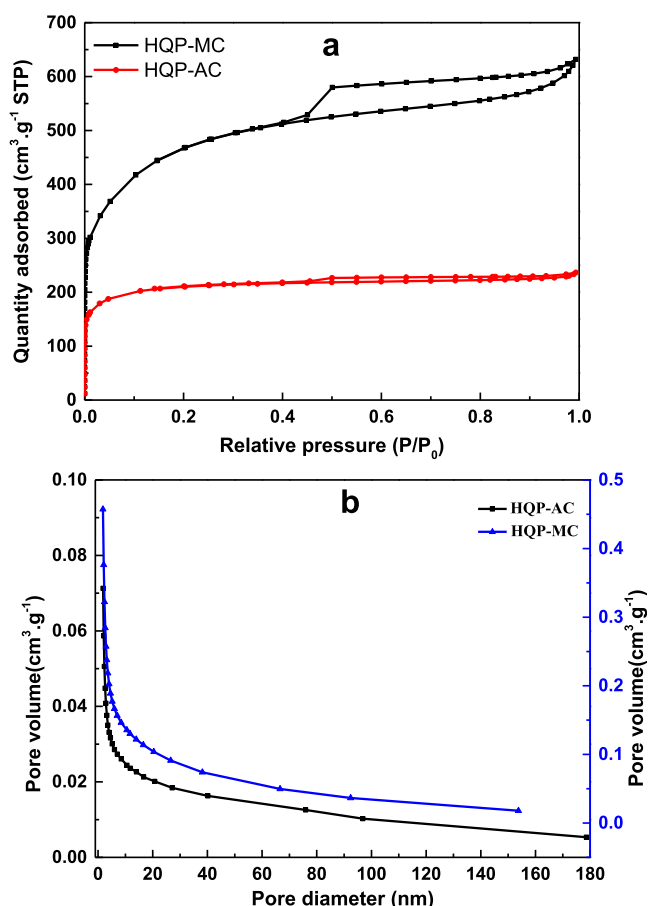
specific surface area and pore volume, facilitating increased adsorption sites and storage capacity. Furthermore, the pore size distribution of the adsorbent plays a critical role in its adsorption efficacy, influencing the accessibility of adsorbate molecules into the adsorbent pores and consequently impacting the adsorption kinetics.

3.2. Adsorption Behavior. *3.2.1. Effects of Initial pH and Adsorbent Dosage.* In order to investigate the impact of pH on the adsorption mechanism, an experimental analysis was conducted utilizing solutions with pH levels spanning from 3.0 to 13.0. The results depicted in Figure 8 illustrate that the

Table 1. Pore Parameters of HQP-AC and HQP-MC

sample	S_{BET} (m²·g⁻¹)	V_t (cm³·g⁻¹)	V_{mes} (cm³·g⁻¹)	V_{mic} (cm³·g⁻¹)	V_{mes}/V_t (%)	V_{mic}/V_t (%)
HQP-AC	648.9	0.6858	0.3659	0.3197	53.3	46.6
HQP-MC	1541.6	1.6868	0.9774	0.6868	57.9	40.7
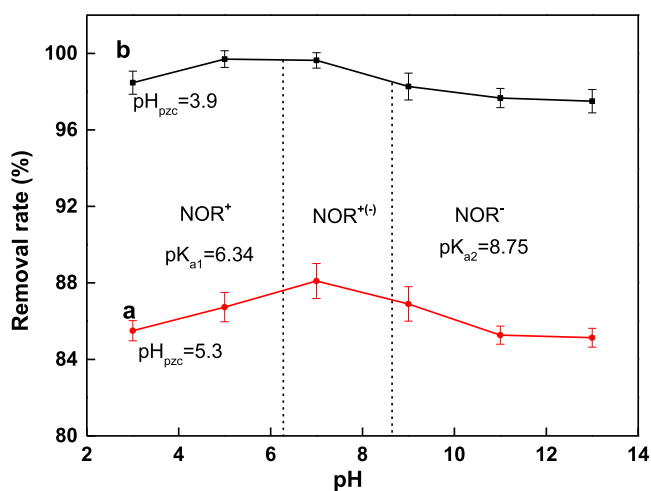
Figure 8. Influence of pH on adsorption performance of HQP-AC (a) and HQP-MC (b) (T = 298 K, c_0 = 100 mg·L⁻¹, t = 10 h).

Figure 9. Adsorption capacity and removal rate under different adsorbent dosages (T = 298 K, pH = 7.0, c_0 = 250 mg·L⁻¹, t = 10 h).

surface of the adsorbent exhibited a positive charge at pH values below the point of zero charge (pH$_{pzc}$), which is recorded at pH values of 5.3 and 3.9 for HQP-AC and HQP-MC, respectively. Conversely, at pH levels exceeding pH$_{pzc}$, the adsorbent surface displayed a negative charge. Regarding NOR, it is present as NOR⁺ at pH values lower than the pK_{a1} of 6.34, transitioning to NOR⁺⁽⁻⁾ within the pH range of 6.34 to 8.75, and finally as NOR⁻ at pH levels surpassing 8.75. Consequently, when the pH falls below the pH$_{pzc}$, there is a repulsion of electrons between the adsorbent and NOR molecules,[4] leading to a lower removal rate. Conversely, when the pH$_{pzc}$ < pH < 8.75, the attraction between electrons of opposing charges intensifies, resulting in an enhanced removal rate. Upon surpassing a pH of 8.75, electron repulsion occurs between particles carrying the same charge. The pH of the solution significantly influences the adsorption process by altering the charge of the adsorbent surface and NOR during the adsorption process.

The quantity of adsorbent utilized is a critical factor influencing adsorbent effectiveness. Hence, an investigation was carried out within the adsorbent dosage range of 0.4 g·L⁻¹ to 2.0 g·L⁻¹. Following the addition of NOR solution with a concentration of 250 mg·L⁻¹, the adsorption process persisted for 10 h at 298 K. The outcomes, as illustrated in Figure 9, demonstrate that the removal efficiency of HQP-AC and HQP-MC increased from 18.5% to 50.5% and from 48% to 98.8%, respectively. Conversely, the adsorption capacity decreased from 151.6 mg·g⁻¹ to 63.1 mg·g⁻¹ and from 306.2 mg·g⁻¹ to 123.6 mg·g⁻¹, respectively. As the adsorption dose increases, the adsorption area and adsorption sites also increase accordingly, while the amount of NOR adsorbed per unit around the adsorbent decreases. At an adsorbent quantity of 1.2 g·L⁻¹, the removal rate exceeded 95%. However, further increments in the quantity resulted in a gradual increase in the removal rate, indicating a low adsorption capacity. Consequently, an adsorbent dose of 1.2 g·L⁻¹ was selected for
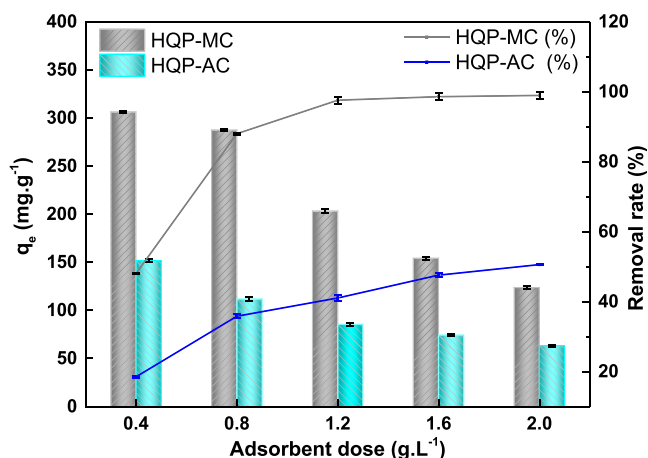
subsequent experiments to explore other factors influencing the adsorption process.

3.2.2. Adsorption Kinetics. Batch adsorption was conducted at different times ranging from 0 to 250 min. The findings depicted in Figure 10 indicate a rapid initial adsorption rate
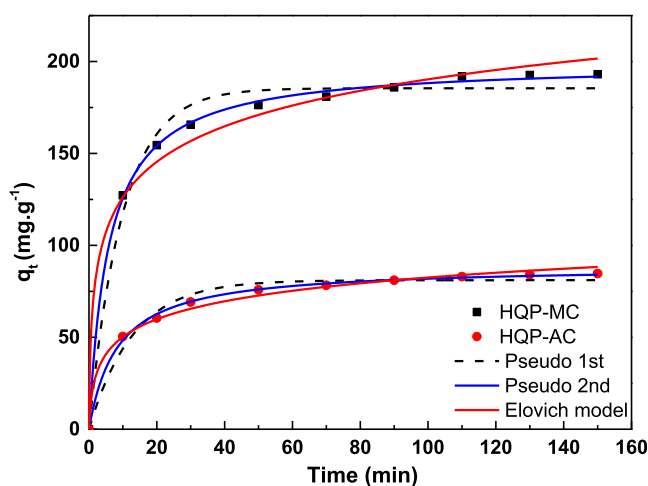
Figure 10. Adsorption kinetic nonlinear fit for NOR adsorption onto HQP-AC and HQP-MC (T = 298 K, pH = 7.0, c_0 = 250 mg·L⁻¹, m = 1.2 g·L⁻¹).

attributed to the active sites present. With prolonged adsorption periods, the active sites of the absorbents became saturated with NOR molecules, leading to a deceleration in the reaction rate until equilibrium was attained. The observed experimental adsorption capacities for HQP-AC and HQP-MC were recorded at 84.7 mg·g⁻¹ and 193.1 mg·g⁻¹, respectively.

The study of adsorption kinetics plays a crucial role in understanding the progression and potential mechanisms involved in the adsorption process. Various nonlinear models such as pseudo-first/second-order kinetic models and the Elovich kinetic model[40] have been utilized to investigate

Table 2. Kinetic Parameters of Pseudo-First-Order, Pseudo-Second-Order, and Elovich Models

adsorbent	first-order kinetic model				second-order kinetic model				Elovich model		
	K_f (min^{-1})	$q_{e,cal.}$ (mg·g^{-1})	R^2	$\triangle q$	k_s (min^{-1})	$q_{e,cal.}$ (mg·g^{-1})	R^2	$\triangle q$	α (mg·g^{-1}·min^{-1})	β (g·mg^{-1})	R^2
HQP-AC	0.077	81.0	0.978	3.7	1.4×10^{-3}	88.7	0.998	4.0	47.2	0.070	0.949
HQP-MC	0.101	185.4	0.982	13.8	8.6×10^{-4}	199.2	0.999	6.1	252.8	0.036	0.924

adsorption kinetics. Analysis presented in Figure 10 and Table 2 demonstrates that the pseudo-second-order kinetic model effectively fits the experimental data, as indicated by the higher correlation coefficient (R^2) and the close alignment between the experimental and theoretical adsorption capacities. Furthermore, the Elovich kinetic model effectively characterizes the adsorption behavior of NOR on HQP-AC and HQP-MC, with notable correlation coefficients (R^2) of 0.949 and 0.924, respectively. Moreover, the substantial values of α (47.2 for HQP-AC, 252.8 for HQP-MC) in comparison to β (0.070 for HQP-AC, 0.036 for HQP-MC) suggest the feasibility and irreversible nature of the adsorption process.[47]

Furthermore, the study also incorporated the intraparticle diffusion model to analyze the adsorption of NOR on HQP-AC and HQP-MC. The adsorption process exhibited three distinct linear stages with varying adsorption rates (shown in Figure 11 and Table 3): external diffusion with a fast
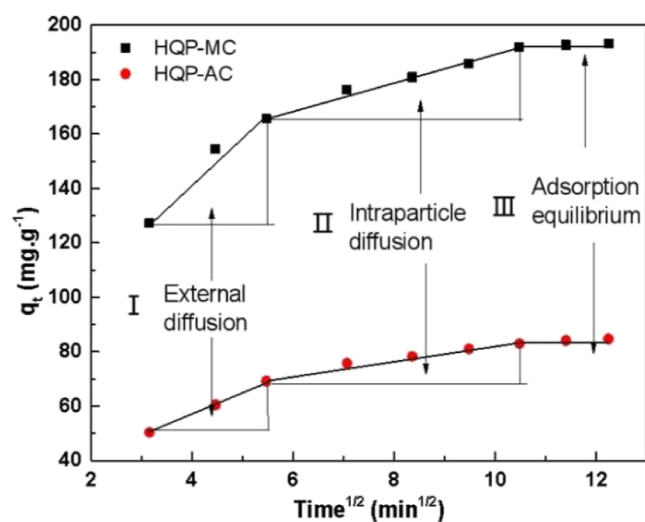
Figure 11. Intraparticle diffusion model for NOR adsorption onto HQP-AC and HQP-MC.

adsorption rate, intraparticle diffusion with a slow adsorption rate, and adsorption equilibrium. Within the first 30 min, a significant portion of the adsorption occurred rapidly, accounting for over 75% of the total adsorption. Subsequently, the rate of reaction decelerated, eventually reaching equilibrium around 90 min. This behavior was attributed to the abundance of active sites and functional groups present on the surfaces of HQP-AC and HQP-MC during the initial adsorption phase. Over time, as the available adsorption sites

on the adsorbents' surfaces became saturated, the adsorption rate declined.

3.2.3. Adsorption Isotherm and Thermodynamics. In investigating the adsorption isotherm of NOR on HQP-AC and HQP-MC, a mixture of 60 mg of adsorbent and a NOR solution with concentrations ranging from 50 mg·L^{-1} to 400 mg·L^{-1} was shaken for 1.5 h at varying temperatures of 298, 308, and 318 K. The results shown in Figure 12 illustrate a notable rise in adsorption as the NOR concentration increased at lower solution concentrations at the same temperature, indicating the presence of a sufficient amount of adsorbent with effective active sites and functional groups. However, the rate of adsorption capacity increment decelerated at higher NOR concentrations due to the saturation of active sites by NOR molecules, leading to equilibrium attainment. Furthermore, an increase in the reaction temperature corresponded to an increase in equilibrium adsorption capacity. The Langmuir model exhibited a strong fit to the experimental data, as evidenced by a high correlation coefficient (R^2) and a minimal deviation between experimental and theoretical adsorption capacities (small Δq), suggesting a monolayer adsorption mechanism.[39,48] Notably, HQP-MC demonstrated higher NOR adsorption capacity compared to other MAC variants documented in the existing literature (Table 5).

The thermodynamic parameters, specifically ΔH, ΔS, and ΔG, were computed and are presented in Table 4. The data illustrates that with an increase in temperature from 298 to 318 K, ΔG remained consistently negative and decreased, while ΔS exhibited a positive trend, indicating the spontaneous nature of the adsorption processes for both adsorbents. Furthermore, the positive ΔH values suggest that the adsorption process is endothermic.[49] Consequently, higher temperatures are advantageous for enhancing spontaneous activity, leading to an increased adsorption capacity.

3.2.4. Actual Water Adsorption and Reusability. In order to investigate the adsorption characteristics of HQP-AC and HQP-MC under realistic aquatic conditions, three distinct water sources were utilized: deionized water, tap water, and Tuman River water. A concentration of 1.2 g·L^{-1} of each adsorbent was added to each water source, which contained 5 mg·L^{-1} of NOR. Consequently, the removal efficiencies for deionized water, tap water, and Tuman River water surpassed 99.0% within 10 min, with the experimental error being less than 1.5%.

The reusability experiment demonstrated that a series of ten repeated adsorption−desorption tests were performed to assess the stability and cyclic adsorption capacity of HQP-AC and HQP-MC. These tests utilized a concentration of 100

Table 3. Parameters and Determination Coefficients of the Intraparticle Diffusion Model

adsorbent	first stage (0−30 min)			second stage (30−90 min)			third stage (90−150 min)		
	K_{d1} (mg·g^{-1}·min$^{-1/2}$)	C_1 (mg·g^{-1})	R^2	K_{d2} (mg·g^{-1}·min$^{-1/2}$)	C_2 (mg·g^{-1})	R^2	K_{d3} (mg·g^{-1}·min$^{-1/2}$)	C_3 (mg·g^{-1})	R^2
HQP-AC	8.1	24.6	0.948	2.6	55.6	0.962	0.969	72.9	0.959
HQP-MC	16.8	75.6	0.997	5.0	139.1	0.985	0.684	184.7	0.947

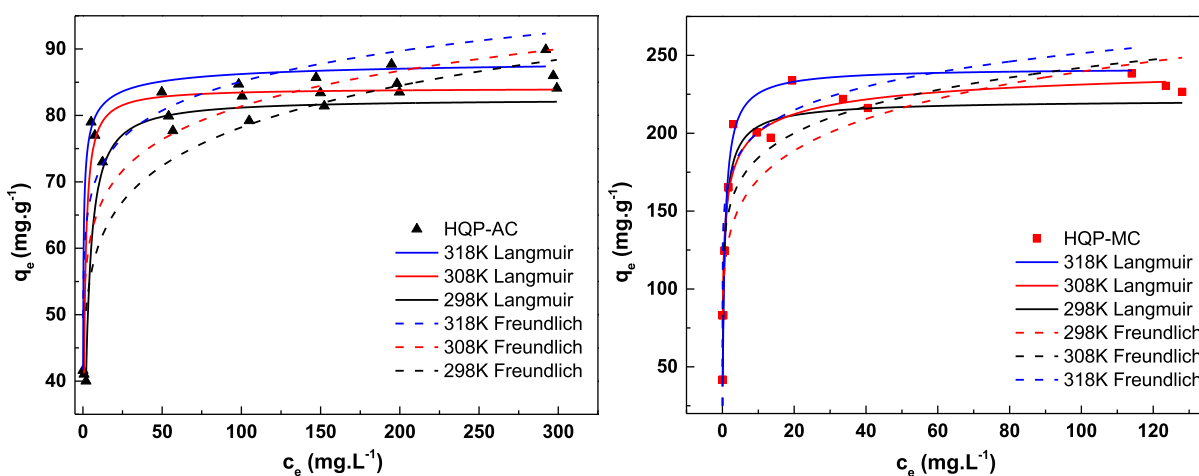**Figure 12.** Adsorption isotherm model for NOR adsorption onto HQP-AC and HQP-MC (pH = 7.0, m = 1.2 g·L^{-1}, t = 90 min).

Table 4. Adsorption Isotherm and Thermodynamic Parameters of HQP-AC and HQP-MC

| adsorbent		HQP-AC			HQP-MC		
		298 K	308 K	318 K	298 K	308 K	318 K
Langmuir	k_L (L·mg^{-1})	0.453	1.273	3.107	1.808	1.624	1.386
	q_m (mg·g^{-1})	82.4	84.1	89.0	221.8	242.1	253.3
	R^2	0.981	0.984	0.988	0.989	0.968	0.987
	$\triangle q$	1.7	1.9	0.9	5.0	11.6	15
Freundlich	k_F (mg·(L$^{1/1-n}$·g))	46.8	53.3	59.9	121.2	140.2	160.5
	$1/n$	0.111	0.091	0.07	0.148	0.118	0.097
	R^2	0.775	0.752	0.855	0.825	0.877	0.626
	$\triangle q$	37.3	32.7	29.1	105.4	90.2	77.8
thermodynamic	$\triangle H$ (kJ·mol^{-1})	35.8			30.7		
	$\triangle S$ (J·mol^{-1}·K^{-1})	135.3			116.4		
	$\triangle G$ (kJ·mol^{-1})	−4.51	−5.87	−7.22	−3.98	−5.15	−6.32
		$y = -4309.2x + 16.27$ (R^2 = 0.986)			$y = -3698.7x + 14.03$ (R^2 = 0.862)		

Table 5. Comparison with Other MAC for NOR Adsorption

raw material	preparation conditions	magnetic substance	magnetic strength (emu·g^{-1})	S_{BET} (m2·g−1)	Q_m (mg·g−1)	contact time (h)	ref
pomelo peel	5 g BC + FeSO$_4$/FeCl$_3$ = 1:2 n/n 1 mol/L NaOH solution was added dropwise to precipitate the iron oxide	γ-Fe$_2$O$_3$	30.60	20.732	5.52	2 h	4
Salix psammophila	4 g of Salix psammophila +1 g of FeCl$_3$·6H$_2$O and 4 g of ZnCl$_2$ in 45 mL of water for 6 h at 60 °C and then pyrolyzed at the setting temperature of 700 °C	γ-Fe$_2$O$_3$	3.57	1348	166	8 h	30
corn stalks, reed stalks, willow branches	raw material: (ZnCl$_2$/FeCl$_3$ = 1:1 m/m) = 5:1 m/m, shaken at 150 rpm for 24 h, then heated at 500 °C in a furnace, and pyrolyzed for 90 min	γ-Fe$_2$O$_3$	ungiven	760−856	3.51−7.62	4 h	37
walnut green husk	HQP-AC powder and ferrocene (m/m, 2:3) mixed with ethanol, sonicated, and pyrolyzed in a tube furnace heated at 800 °C for 4 h under nitrogen protection	Fe$_3$O$_4$	11.5	1541.6	226.8 (298 K)	1.5 h	this work

mg·L^{-1} of NOR and an adsorbent concentration of 1.2 g·L^{-1}, conducted at a temperature of 298 K. Following each adsorption phase, HQP-AC and HQP-MC were isolated through centrifugation and an external magnet, respectively. As depicted in Figure 13, HQP-MC exhibited a sustained removal efficiency of 80.5% after 10 cyclic adsorption−desorption tests, surpassing HQP-AC, which experienced a decline in removal efficiency after the fifth cycle. These findings suggest that magnetized activated carbon, characterized by high reusability and rapid separation capabilities, exhibits the potential for applications aimed at removing contaminants from water sources.

3.3. Mechanism of Adsorption. The adsorption mechanisms of NOR onto HQP-AC and HQP-MC are depicted in Figure 14. When the pH is below the point of zero charge (pH$_{pzc}$), the surfaces of HQP-AC and HQP-MC exhibit a positive charge. In this scenario, the nitrogen atom in the NOR molecule accepts a proton, resulting in the formation of positively charged species NOR$^+$. Consequently, electrostatic repulsion occurs between the adsorbents and the NOR$^+$. The primary adsorption processes under these conditions include pore filling, $\pi-\pi$ interactions between the aromatic rings of NOR and the adsorbents, and hydrogen bonding between the hydroxyl (OH) and amine (NH) groups on the adsorbents and the nitrogen, oxygen, and fluorine atoms in NOR. When
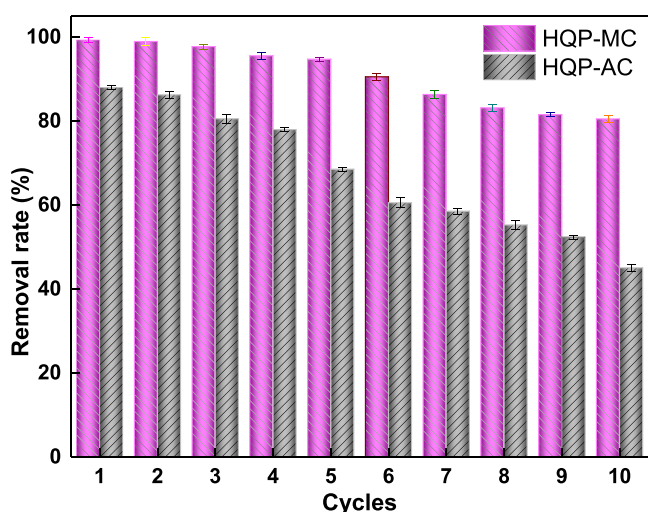
Figure 13. Reusability of HQP-AC and HQP-MC for NOR ($T = 298$ K, pH = 7.0, $c_0 = 100$ mg·L^{-1}, $m = 1.2$ g·L^{-1}).
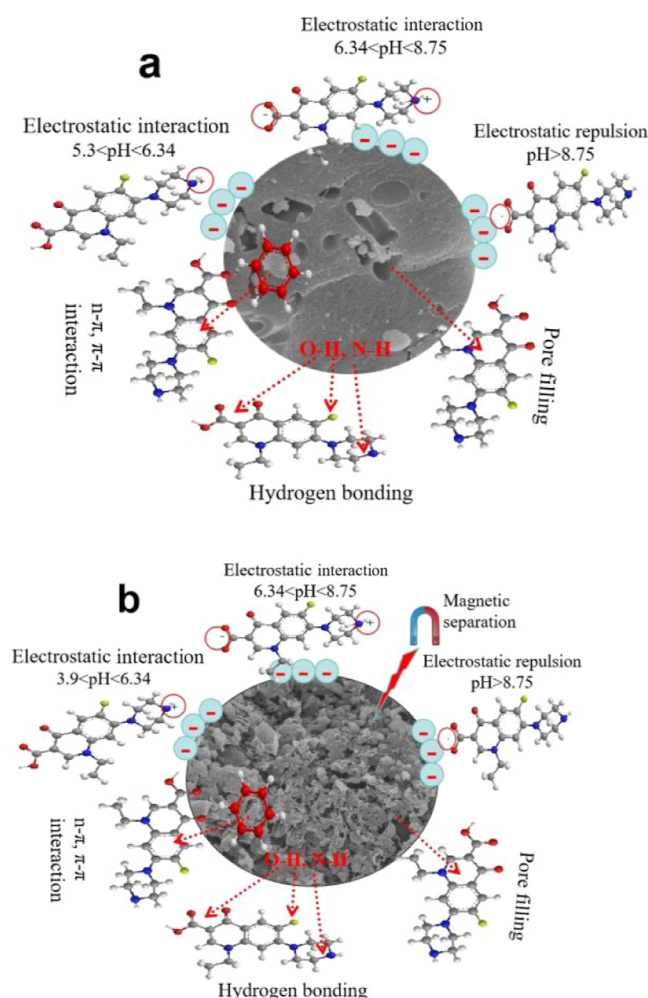
Figure 14. Schematic illustration of the adsorption mechanism of NOR onto HQP-AC (a) and HQP-MC (b).

the pH is within the range where pH$_{pzc}$ < pH < pK_{a1} (NOR), the surfaces of HQP-AC and HQP-MC exhibit a negative charge. Consequently, the predominant mechanisms of adsorption include electrostatic attraction, pore filling, π–π interactions between the aromatic rings of NOR and the

adsorbents, and hydrogen bonding between the hydroxyl (OH) and amine (NH) groups on the adsorbents and the nitrogen, oxygen, and fluorine atoms present in NOR. In the pH range where pK_{a1} < pH < pK_{a2}, NOR exists in a zwitterionic form, and the primary adsorption processes remain similar, involving electrostatic attraction, pore filling, π–π interactions, and hydrogen bonding. When the pH exceeds pK_{a2}, the carboxylic acid group (−COOH) in NOR loses a proton, resulting in the formation of NOR$^-$. In this scenario, the main adsorption processes shift to pore filling, π–π interactions between the aromatic rings of NOR and the adsorbents, and hydrogen bonding between the OH and NH groups on the adsorbents and the N, O, and F atoms in NOR.

4. CONCLUSIONS

A high-quality porous magnetic activated carbon (HQP-MC) was synthesized using walnut green husk and ferrocene as precursors, demonstrating remarkable characteristics such as a specific surface area of 1541.66 m^2·g^{-1}, pore volume of 1.6868 cm^3·g^{-1}, and magnetic saturation strength of 11.5 emu·g^{-1}. Comparative analysis of HQP-MC and HQP-AC for the adsorption of NOR revealed that HQP-MC exhibited a significant adsorption capacity of 226.8 mg·g^{-1} at 298 K, along with a reusability rate of 80.5% over 10 cycles. The adsorption kinetics were well-described by the pseudo-second-order model, while the Langmuir model effectively represented the adsorption isotherm. Thermodynamic analysis indicated the endothermic, spontaneous, and entropy increment nature of the adsorption process, with negative Gibbs free energy (ΔG < 0), positive enthalpy change (ΔH > 0), and positive entropy change (ΔS > 0). Furthermore, the magnetic properties of HQP-MC facilitate easy separation using an external magnet, eliminating the need for conventional separation methods such as centrifugation or filtration. This study not only introduces a novel approach for producing magnetic carbon materials from agricultural byproducts but also accomplishes the objective of "treating pollutants with waste and turning waste into treasure".

■ AUTHOR INFORMATION

Corresponding Author

Abdukader Abdukayum − *Xinjiang Key Laboratory of Novel Functional Materials Chemistry, Kashi University, Kashi 844000, PR China;* orcid.org/0000-0002-2009-1179; Email: abdukadera@sina.com

Authors

Resalat Yimin − *Xinjiang Key Laboratory of Novel Functional Materials Chemistry, Kashi University, Kashi 844000, PR China;* orcid.org/0009-0003-8504-9902

Reyangul Abla − *Laboratory of Xinjiang Native Medicinal and Edible Plant Resources Chemistry, College of Chemistry and environmental Science, Kashi University, Kashi 844000, PR China*

Gulbagar Dawut − *Xinjiang Key Laboratory of Novel Functional Materials Chemistry, Kashi University, Kashi 844000, PR China*

Bin Xiong − *Xinjiang Key Laboratory of Novel Functional Materials Chemistry, Kashi University, Kashi 844000, PR China*

Complete contact information is available at:
https://pubs.acs.org/10.1021/acsomega.4c05032

Author Contributions

Resalat Yimin: Conceptualization, methodology, and writing—original draft preparation. Reyangul Abla: Data curation and formal analysis. Gulbahar Dawut: Data curation and formal analysis. Abdukader Abdukayum: Supervision and writing—review and editing. Bin Xiong: Methodology and validation.

Notes

The authors declare no competing financial interest.

■ REFERENCES

(1) Martinez, J. L. Environmental pollution by antibiotics and by antibiotic resistance determinants. *Environ. Pollut.* **2009**, *157*, 2893−2902.

(2) Shao, J.; Guo, F. Y.; Hao, Y. C.; Liu, J. P.; Liu, Y. J. Adsorption behaviors of norfloxacin by activated carbon derived from waste coffee grounds (in Chinese). *Chem. Res. Appl.* **2022**, *34*, 2807−2813.

(3) Zhou, H. J.; Wang, Z.; Gao, C. L.; Sun, Q. Q.; Liu, J.; She, D. Synthesis of honeycomb lignin-based biochar and its high-efficiency adsorption of norfloxacin. *Bioresour. Technol.* **2023**, *369*, 128402.

(4) Wang, J. P.; Zhang, M.; Zhou, R. J.; Li, J. Y.; Zhao, W.; Zhou, J. H. Adsorption characteristics and mechanism of norfloxacin in water by γ-Fe$_2$O$_3$@BC. *Water Sci. Technol.* **2020**, *82*, 242−254.

(5) Fang, N.; He, Q.; Sheng, L.; Xi, Y. H.; Zhang, L. P.; Liu, H. W.; Cheng, H. C. Toward broader applications of iron ore waste in pollution control: Adsorption of norfloxacin. *J. Hazard. Mater.* **2021**, *418*, 126273.

(6) Hacıosmanoğlu, G. G.; Arenas, M.; Mejías, C.; Martín, J.; Santos, J. L.; Aparicio, I.; Alonso, E. Adsorption of Fluoroquinolone Antibiotics from Water and Wastewater by Colemanite. *Int. J. Environ. Res. Publ. Health* **2023**, *20*, 2646.

(7) Zhao, L.; Dong, Y. H.; Wang, H. Residues of veterinary antibiotics in manures from feedlot livestock in eight provinces of China. *Sci. Total Environ.* **2010**, *408*, 1069−1075.

(8) Amorim, C. L.; Moreira, I. S.; Maia, A. S.; Tiritan, M. E.; Castro, P. M. L. Biodegradation of ofloxacin, norfloxacin, and ciprofloxacin as single and mixed substrates by Labrys portucalensis F11. *Appl. Microbiol. Biotechnol.* **2014**, *98*, 3181−3190.

(9) Li, X. Y.; Jiang, Y. Y.; Chen, T. Y.; Zhao, P.; Niu, S.; Yuan, M. Z.; Ma, X. L. Adsorption of norfloxacin from wastewater by biochar with different substrates. *Environ. Geochem. Health* **2023**, *45*, 3331−3344.

(10) Li, N.; He, M. T.; Lu, X. K.; Liang, L.; Li, R.; Yan, B. B.; Chen, G. Y. Enhanced norfloxacin degradation by visible-light-driven Mn3O4/γ-MnOOH photocatalysis under weak magnetic field. *Sci. Total Environ.* **2021**, *761*, 143268.

(11) Xue, L.; Zhao, C. X.; Liu, J. M.; Zhong, N. Y.; Zhang, J. H.; Huang, K. M. Microwave electrodeless UV light source combine ozone generation with photocatalytic simultaneous degradation of norfloxacin. *Chem. Eng. Process.* **2023**, *186*, 109325.

(12) Tang, Q. Y.; Wei, X.; Wang, C. C. Photocatalysis-activated SR-AOP over ZIF-NC/PTCDA composites for boosted norfloxacin degradation (in Chinese). *J. Mater. Eng.* **2023**, *51*, 48−56.

(13) Feng, G. Y.; Su, R. K.; Yan, Z. G.; Li, S. P.; Xu, M.; Wang, C. W.; Li, Y. B. Polyelectrolyte complex nanofiltration membranes with low MWCO for pharmaceuticals removal. *Sep. Purif. Technol.* **2023**, *325*, 124669.

(14) Vinayagam, V.; Murugan, S.; Kumaresan, R.; Narayanan, M.; Sillanpaa, M.; Viet N Vo, D.; Kushwaha, O. S.; Jenis, P.; Potdar, P.; Gadiya, S. Sustainable adsorbents for the removal of pharmaceuticals from wastewater: A review. *Chemosphere* **2022**, *300*, 134597.

(15) Nordin, A. H.; Norfarhana, A. S.; Noor, S. F.; Paiman, S. H.; Nordin, M. L.; Husna, S. M. N.; Ilyas, R. A.; Ngadi, N.; Bakar, A. A.; Ahmad, Z.; Azami, M. S.; Nawawi, W. I.; Nabgan, W. Recent Advances in Using Adsorbent Derived from Agricultural Waste for Antibiotics and Non-Steroidal Anti-Inflammatory Wastewater Treatment: A Review. *Separations* **2023**, *10*, 300.

(16) Yu, M. X.; Zhu, B. W.; Yu, J. X.; Wang, X. T.; Zhang, C.; Qin, Y. A biomass carbon prepared from agricultural discarded walnut green husk: investigations into its adsorption characteristics of heavy metal ions in wastewater treatment. *Biomass Convers. Biorefin.* **2023**, *13*, 12833−12847.

(17) Othmani, A.; Magdouli, S.; Kumar, P. S.; Kapoor, A.; Chellam, P. V.; Gökkuş, O.∴ Agricultural waste materials for adsorptive removal of phenols, chromium (VI) and cadmium (II) from wastewater: A review. *Environ. Res.* **2022**, *204* (A), 111916.

(18) Zhao, M. M.; Liu, X.; Huang, Y. Q.; Ma, X. J.; Yu, L. L.; Sun, B. Q.; Li, D. N. Preparation and Ethylene Adsorption Performance of Full-component Wood-basedActivated Carbon Spheres(in Chinese). *Packag. Eng.* **2023**, *44*, 96−103.

(19) Xu, T. T.; Du, J. K.; Zhang, J.; David, W.; Liu, P.; Faheem, M.; Zhu, X. W.; Yang, J. W.; Bao, J. G. Microbially-mediated synthesis of activated carbon derived from cottonseed husks for enhanced sulfanilamide removal. *J. Hazard. Mater.* **2022**, *426*, 127811.

(20) Qin, Y.; Chai, B.; Wang, C. L.; Yan, J. T.; Fan, G. Z.; Song, G. S. Removal of tetracycline onto KOH-activated biochar derived from rape straw: Affecting factors, mechanisms and reusability inspection. *Colloids Surf. A Physicochem. Eng. Asp.* **2022**, *640*, 128466.

(21) Mohan, D.; Sarswat, A.; Singh, V. K.; Alexandre-Franco, M.; Pittman, C. U., Jr Development of magnetic activated carbon from almond shells for trinitrophenol removal from water. *Chem. Eng. J.* **2011**, *172*, 1111−1125.

(22) Wong, K. T.; Yoon, Y.; Jang, M. Enhanced Recyclable Magnetized Palm Shell Waste-Based Powdered Activated Carbon for the Removal of Ibuprofen: Insights for Kinetics and Mechanisms. *PLoS One* **2015**, *10*, No. e0141013.

(23) Wu, T.; Yao, C. F.; Hao, S. Y.; Chen, W. X.; Yu, M.; Fan, H. Adsorption performance of nano-hydroxyferric modified activated Carbon for methylene blue (in Chinese). *Environ. Pollut Control* **2023**, *45*, 1096−1100.

(24) Maguana, Y. E.; Elhadiri, N.; Benchanaa, M.; Chikri, R. Activated Carbon for Dyes Removal: Modeling and Understanding the Adsorption Process. *J. Chem.* **2020**, *2020*, 2096834.

(25) Astuti, W.; Sulistyaningsih, T.; Kusumastuti, E.; Thomas, G. Y. R. S.; Kusnadi, R. Y. Thermal conversion of pineapple crown leaf waste to magnetized activated carbon for dye removal. *Bioresour. Technol.* **2019**, *287*, 121426.

(26) Sun, H. W.; Yang, J. J.; Wang, Y.; Liu, Y. C.; Cai, C. J.; Davarpanah, A. Study on the Removal Efficiency and Mechanism of Tetracycline in Water Using Biochar and Magnetic Biochar. *Coatings* **2021**, *11*, 1354.

(27) Pereira, D.; Rocha, L. S.; Gil, M. V.; Otero, M.; Silva, N. J. O.; Esteves, V. I.; Calisto, V. In situ functionalization of a cellulosic-based activated carbon with magnetic iron oxides for the removal of carbamazepine from wastewater. *Environ. Sci. Pollut. Res.* **2021**, *28*, 18314−18327.

(28) Yang, H. W.; Zhou, J.; Yang, E. X.; Li, H. X.; Wu, S. J.; Yang, W.; Wang, H. Magnetic Fe$_3$O$_4$-N-doped carbon sphere composite for tetracycline degradation by enhancing catalytic activity for peroxymonosulfate: A dominant non-radical mechanism. *Chemosphere* **2021**, *263*, 128011.

(29) Hu, P. D.; Long, M. C. Cobalt-catalyzed sulfate radical-based advanced oxidation: A review on heterogeneous catalysts and applications. *Appl. Catal., B* **2016**, *181*, 103−117.

(30) Liu, P. L.; Li, H. P.; Liu, X.; Wan, Y. B.; Han, X. L.; Zou, W. H. Preparation of magnetic biochar obtained from one-step pyrolysis of salix mongolica and investigation into adsorption behavior of

sulfadimidine sodium and norfloxacin in aqueous solution. *J. Dispersion Sci. Technol.* **2020**, *41*, 214−226.

(31) Feng, Z. Q.; Chen, H. L.; Li, H. Q.; Yuan, R. F.; Wang, F.; Chen, Z. B.; Zhou, B. H. Preparation, characterization, and application of magnetic activated carbon for treatment of biologically treated papermaking wastewater. *Sci. Total Environ.* **2020**, *713*, 136423.

(32) Chen, W. H.; Hoang, A. T.; Nižetić, S.; Pandey, A.; Cheng, C. K.; Luque, R.; Ong, H. C.; Thomas, S.; Nguyen, X. P. Biomass-derived biochar: From production to application in removing heavy metal-contaminated water. *Process Saf. Environ. Prot.* **2022**, *160*, 704−733.

(33) Tang, J.; Wang, Y. J.; Ma, J.; Chen, Y. J.; Chen, M. High-density Co-Nx sites anchored on biomass-based carbon nanotubes for efficient removal of plant viruses in water. *J. Environ. Chem. Eng.* **2024**, *12*, 113022.

(34) Yin, Y.; Wu, X. W.; Huang, C. Y.; Dong, Y. L.; Liu, J. Q.; Tan, Y.; Liang, H.; Yang, S. Y. Microwave synthesized novel biomass carbon dots applied in the fluorescent detection of crystal violet. *Luminescence* **2024**, *39*, No. e4778.

(35) Allende, S.; Liu, Y.; Zafar, M. A.; Jacob, M. V. Synthesis and application of biomass-based graphene oxide using microwave-assisted pyrolysis method. *Nano-Struct. Nano-Objects* **2024**, *40*, 101338.

(36) Zhang, S. F.; Wang, W. R.; Yan, X.; Wang, R. M.; Nie, L. Y.; Yu, J. Study on adsorption of zinc ions by modified activated carbon from walnut green peel (in Chinese). *China Nonferrous Metall.* **2024**, *53*, 125−131.

(37) Wang, B.; Jiang, Y. S.; Li, F. Y.; Yang, D. Y. Preparation of biochar by simultaneous carbonization, magnetization and activation for norfloxacin removal in water. *Bioresour. Technol.* **2017**, *233*, 159−165.

(38) Zhong, M. J.; Liu, X. G.; Ma, J. F.; Shang, L. L. Bamboo-Activated Carbon Synthesized by One-Pot Pyrolysis and FeCl$_2$ Activation for the Removal of Cr(VI) in Aqueous Solutions. *Water* **2023**, *15*, 1891.

(39) Wang, Q. Y.; Fagbohun, E. O.; Zhu, H. K.; Hussain, A.; Wang, F.; Cui, Y. B. One-step synthesis of magnetic asphalt-based activated carbon with high specific surface area and adsorption performance for methylene blue. *Sep. Purif. Technol.* **2023**, *321*, 124205.

(40) AlHumaidan, F. S.; Hauser, A.; Rana, S. M.; Lababidi, M. S. H.; Behbehani, M. Changes in asphaltene structure during thermal cracking of residual oils: XRD study. *Fuel* **2015**, *150*, 558−564.

(41) Liu, Y.; Zhu, Z. S.; Cheng, Q.; Ren, H. D.; Wang, S.; Zhao, Y.; Li, J. J.; Zhu, J. B.; Kong, L. B. One-step preparation of environment-oriented magnetic coal-based activated carbon with high adsorption and magnetic separation performance. *J. Magn. Magn. Mater.* **2021**, *521*, 167517.

(42) Lin, X. C.; Sheng, Z.; He, J.; He, X.; Wang, C. H.; Gu, X. H.; Wang, Y. G. Preparation of isotropic spinnable pitch with high-spinnability by cocarbonization of coal tar pitch and bio-asphalt. *Fuel* **2021**, *295*, 120627.

(43) Patawat, C.; Silakate, K.; Chuan-Udom, S.; Supanchaiyamat, N.; Hunt, A. J.; Ngernyen, Y. Preparation of activated carbon from Dipterocarpus alatus fruit and its application for methylene blue adsorption. *RSC Adv.* **2020**, *10*, 21082−21091.

(44) Li, L.; Lin, X. C.; Zhang, Y. K.; Dai, J. Z.; Xu, D. P.; Wang, Y. G. Characteristics of the mesophase and needle coke derived from the blended coal tar and biomass tar pitch. *J. Anal. Appl. Pyrol.* **2020**, *150*, 104889.

(45) Raji, Y.; Nadi, A.; Mechnou, I.; Saadouni, M.; Cherkaoui, O.; Zyade, S. High adsorption capacities of crystal violet dye by low-cost activated carbon prepared from Moroccan Moringa oleifera wastes: Characterization, adsorption and mechanism study. *Diam. Relat. Mater.* **2023**, *135*, 109834.

(46) Thommes, M.; Kaneko, K.; Neimark, A. V.; Olivier, J. P.; Rodriguez-Reinoso, F.; Rouquerol, J.; Sing, K. S. Physisorption of gases, with special reference to the evaluation of surface area and pore size distribution (IUPAC Technical Report). *Pure Appl. Chem.* **2015**, *87*, 1051−1069.

(47) Fagbohun, E. O.; Wang, Q. Y.; Spessato, L.; Zheng, Y. H.; Li, W. L.; Olatoye, A. G.; Cui, Y. B. Physicochemical regeneration of industrial spent activated carbons using a green activating agent and their adsorption for methyl orange. *Surf. Interface* **2022**, *29*, 101696.

(48) Chishti, A. N.; Ni, L.; Guo, F.; Lin, X. Y.; Liu, Y.; Wu, H. Y.; Chen, M.; Diao, G. W. Magnetite-Silica core-shell nanocomposites decorated with silver nanoparticles for enhanced catalytic reduction of 4-nitrophenol and degradation of methylene blue dye in the water. *J. Environ. Chem. Eng.* **2021**, *9*, 104948.

(49) Yu, M. X.; Zhu, B. W.; Yu, J. X.; Wang, X. T.; Zhang, C.; Qin, Y. A biomass carbon prepared from agricultural discarded walnut green husk: investigations into its adsorption characteristics of heavy metal ions in wastewater treatment. *Biomass Convers. Biorefin.* **2023**, *13*, 12833−12847.